remote sensing

MDPI

Article

Vertical Structures and Macro-Microphysical Characteristics of Southwest Vortex Precipitation over Sichuan, China

Yanxia Liu [1,2,3], Jun Wen [3,*], Jiafeng Zheng [4,5] and Hao Wang [4]

[1] Northwest Institute of Eco-Environment and Resources, Chinese Academy of Sciences, Lanzhou 730000, China; liuyx@cuit.edu.cn
[2] University of Chinese Academy of Sciences, Beijing 100039, China
[3] Plateau Atmosphere and Environment Key Laboratory of Sichuan Province/School of Atmospheric Sciences, Chengdu University of Information Technology, Chengdu 610225, China
[4] College of Electronic Engineering (College of Meteorological Observation), Chengdu University of Information Technology, Chengdu 610225, China; zjf1988@cuit.edu.cn (J.Z.); wh@cuit.edu.cn (H.W.)
[5] Key Laboratory of Intelligent Meteorological Observation Technology, China Meteorological Administration, Beijing 100081, China
* Correspondence: jwen@cuit.edu.cn

Highlights

What are the main findings?

- Southwest China vortex (SWV) precipitation is found to vary significantly across life-cycle stages, with clear differences in vertical structure, precipitation intensity, and the associated macro-microphysical evolution.
- SWV precipitation exhibits distinct type-dependent structural and microphysical signatures, reflected in vertical organization, radar-echo characteristics, and drop size distribution properties and dominant warm-rain processes.

What are the implications of the main findings?

- The stage- and type-resolved vertical microphysical signatures provide satellite-based observational benchmarks for evaluating and improving cloud microphysics parameterizations over complex terrain.
- The process diagnostics (coalescence, breakup, and evaporation-size sorting) provide physically interpretable constraints that support improved numerical prediction of SWV-related rainfall and associated hazards.

Abstract

The Southwest China vortex (SWV) is a high-impact mesoscale cyclonic vortex that typically originates over Sichuan Province, China, and frequently produces hazardous rainfall. Yet systematic knowledge of the structural and microphysical properties of SWV precipitation remains insufficiently quantified. Using Global Precipitation Measurement Dual-frequency Precipitation Radar (GPM/DPR) observations from 2014 to 2022, this study investigates the vertical structure and macro- and microphysical characteristics of SWV precipitation, and quantifies their differences across life-cycle stages and precipitation types. The mature stage is characterized by higher echo tops, stronger radar reflectivity, higher strong-echo altitudes, and larger near-surface rainfall, together with a clearer melting-layer bright band and a stronger post-melting shift toward larger drops and lower number concentrations. The developing stage is weakest and shows the largest fraction of coalescence–breakup balance signatures, whereas the dissipating stage features enhanced evaporation- and breakup-related signals. Among precipitation types, deep strong convection exhibits the greatest vertical extent with enhanced ice/mixed-phase growth; stratiform precipitation

Check for updates

Academic Editor: Yuriy Kuleshov

Received: 4 January 2026
Revised: 1 February 2026
Accepted: 5 February 2026
Published: 6 February 2026

Copyright: © 2026 by the authors. Licensee MDPI, Basel, Switzerland. This article is an open access article distributed under the terms and conditions of the Creative Commons Attribution (CC BY) license.

produces stronger radar echoes and higher rainfall rates than deep weak convection despite similar echo-top heights; and shallow precipitation is characterized by smaller drops, higher concentrations, and active warm-rain spectral evolution. These findings provide satellite-based constraints for microphysics parameterization evaluation and improved numerical prediction of SWV-related rainfall over complex terrain.

Keywords: Southwest China vortex; precipitation; vertical structure; macro- and microphysical characteristics; GPM/DPR

1. Introduction

The Southwest China vortex (SWV) is a meso-α-scale cyclonic vortex that typically forms near the 700–850-hPa levels over the lee side of the eastern Tibetan Plateau in southwestern China (99–109°E, 26–33°N), driven by the combined effects of complex topography, diabatic processes, and large-scale circulation. The SWV is the primary synoptic system responsible for heavy rainfall over Sichuan Province and can further intensify and propagate eastward under favorable large-scale circulation conditions, triggering widespread thunderstorms and rainstorms over downstream regions including the Yangtze River basin, Northeast China, Northern China, Central China, and Southern China [1–4]. Climatological studies have shown that SWVs mainly originate from three major source regions in Sichuan, namely Jiulong (JL), the Sichuan Basin, and Xiaojin (XJ) (Figure 1), and that these source regions exhibit systematic differences in occurrence frequency, propagation pathways, and affected areas [5–7].

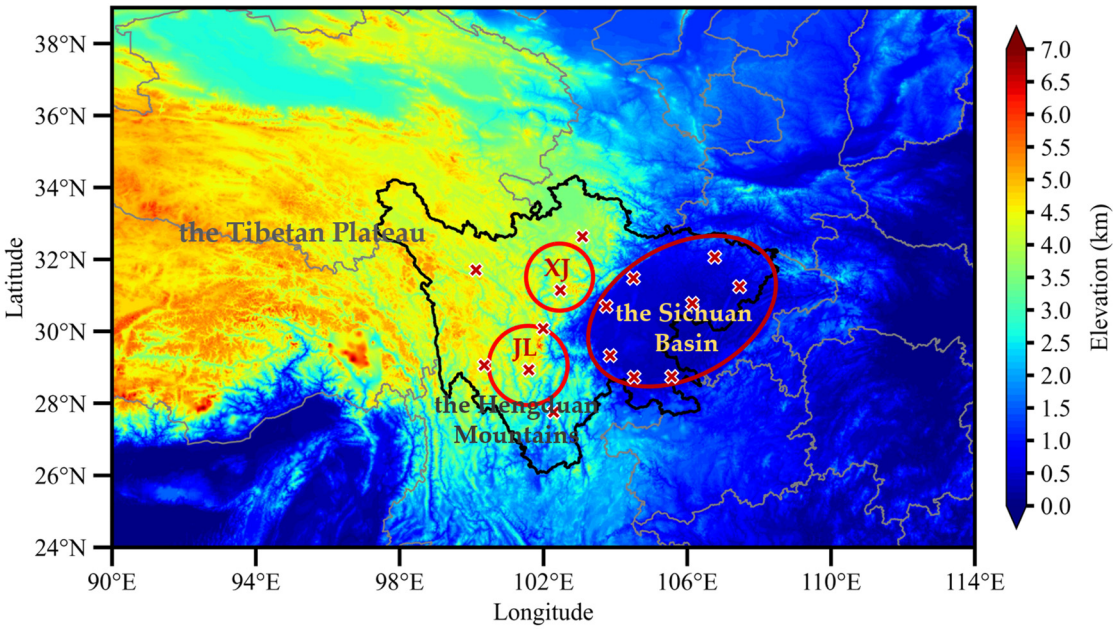

Figure 1. Terrain of Sichuan Province and its surroundings. The bold black line represents the provincial boundary of Sichuan Province. The red solid ellipses denote the three SWV source regions of Jiulong (JL), Xiaojin (XJ), and the Sichuan Basin. The red crosses represent the locations of the ground-based disdrometers.

The factors controlling the formation and development of SWVs are highly complex and strongly multiscale, involving the large-scale circulation background, the dynamical and thermal forcing of the Tibetan Plateau and the Hengduan Mountains, local thermal forcing, and internal vortex-scale evolution. In terms of formation mechanisms, an SWV can

be regarded as a lee vortex on the eastern flank of the Tibetan Plateau and the Hengduan Mountains. When midlatitude westerlies or the summer southwesterly monsoon impinge upon the Hengduan Mountains with a favorable incident angle, the airflow is forced to ascend on the windward slopes and can form a separated shear layer and a recirculation region on the lee side, thereby generating a low-level vortex over the eastern Tibetan Plateau and the Sichuan Basin [8–11].

Differential heating over the plateau and latent heat release from deep convection can further enhance potential vorticity and promote the transition from a shallow, thermally driven vortex into a deep, dynamically driven system. Eastward-moving Tibetan Plateau vortices that migrate off the plateau and merge with low-level vortices over the Sichuan Basin provide an additional important mechanism for the formation and intensification of some strong SWVs [12–18]. Meanwhile, the warm and moist boundary layer over the Sichuan Basin, the southern-branch low-level jet, and moisture transport from the Bay of Bengal and the South China Sea supply abundant moisture and convective instability for SWVs. The development of low-level warm advection and symmetric instability is often closely associated with vortex intensification and the occurrence of heavy rainfall [19–22].

In recent years, observations from surface meteorological station networks and ground-based weather radars have substantially improved our understanding of the precipitation characteristics associated with SWVs. Observational analyses have shown that SWV-induced rainstorms are frequently accompanied by high-frequency, short-duration heavy rainfall bands that develop and propagate along the vortex axis from the southwestern Sichuan Basin to downstream regions, and that the relative contributions of convective and stratiform precipitation exhibit systematic differences among different stages of the vortex life cycle [5,23,24]. In typical intense SWV cases, convective cells can extend to the upper troposphere, while a pronounced radar bright band is often observed in the stratiform region near the 0 °C level. Stratiform and convective precipitation differ markedly in their vertical extent, echo-top height, and hydrometeor phase composition. Overall, SWV rainstorms tend to exhibit a mixed structure characterized by deep stratiform cloud shields embedded with multiple convective bands, and phase transitions between ice particles and supercooled water play a key role in modulating surface rainfall intensity [25]. However, owing to the highly complex orography, surface station networks and ground-based weather radars remain relatively sparse over southwestern China, and radar observations are severely affected by terrain blocking, leading to substantial limitations in depicting the three-dimensional structure of SWV precipitation [26].

With the development of spaceborne active microwave remote sensing, precipitation radars onboard polar-orbiting satellites, such as the Tropical Rainfall Measuring Mission Precipitation Radar (TRMM/PR) and the Global Precipitation Measurement Dual-frequency Precipitation Radar (GPM/DPR), have provided an important perspective for documenting precipitation structure and physical characteristics over complex terrain, thereby complementing ground-based radar observations that are sparse and affected by terrain blocking in this region. Based on these observations, Jiang et al. (2014, 2015) [27,28] reported that SWV-induced rainfall typically manifests as a mesoscale system composed of a primary rainband accompanied by scattered convective cells. Although convective precipitation accounts for a smaller fraction of samples, it features much higher rain rates and cloud tops that can exceed 16 km, with peak precipitation rates concentrated between 2 and 6 km, and precipitation below 6 km contributes most to the total rainfall. Compared with Tibetan Plateau vortices, SWVs exhibit stronger convection and a larger contribution from precipitation in the 8–12 km layer, indicative of more evident deep-convective characteristics. Xiang et al. (2021) [4] further found that precipitation below the melting layer generally contributes more than 60% of the total rainfall, and that a larger fraction of convective

precipitation corresponds to stronger latent heating; in typical cases, latent heating on the eastern flank of the SWV is stronger than on the western flank. Synthesizing previous studies, Li and Chen (2018) [29] and Xiang et al. (2023) [30] suggested that SWV precipitation generally exhibits a dual nature characterized by both prominent warm-rain processes and intense deep convection, implying highly complex cloud-precipitation microphysics. More generally, cloud-precipitation systems undergo distinct thermodynamic and dynamical evolutions across different life-cycle stages, and therefore often exhibit pronounced differences in vertical structure as well as in macro- and microphysical characteristics [31–33]. Such life-cycle-dependent variations have been documented for a wide range of precipitation systems worldwide. For example, Zhang and Fu (2018) reported systematic differences in the vertical structure and microphysical properties of spring–summer precipitation over eastern China across different cloud life stages [34], while Sun et al. (2020) presented analogous results for Meiyu-season rainfall over central China based on GPM/DPR observations [35].

Knowledge of precipitation vertical structure and associated macroscopic and microphysical parameters is fundamental for understanding the development and evolution of SWV rainstorms and for improving numerical prediction of SWVs and their associated rainfall. Although previous studies have made valuable progress through case diagnoses, simulation studies, and various remote-sensing observations [4,27,28,30,36–38], they have mostly focused on single or a few typical or extreme SWV events. Consequently, the generality and robustness of the reported structural and microphysical features remain unclear, and systematic analyses based on long-term observations are still lacking. To address this gap, this study uses GPM/DPR observations from 2014 to 2022 to identify and screen all SWV events affecting Sichuan Province during this 9-year period. We then comprehensively analyze the vertical structure and the macro- and microphysical characteristics of precipitation, as well as their differences, from the dual perspectives of different SWV development stages and different precipitation types. The remainder of this manuscript is organized as follows. Section 2 describes the study region, data, and methodology. Section 3 presents the results in detail. Section 4 compares and discusses our findings with those for other rainy seasons or typical precipitation systems in China. Section 5 summarizes the main conclusions.

2. Study Region, Data, and Methodology

2.1. Study Region

As shown in Figure 1, this study focuses on Sichuan Province in Southwest China, the main region where SWVs form and exert their influence. Sichuan Province has highly distinctive topography: the western part extends along the eastern slopes of the Tibetan Plateau and the Hengduan Mountains, with mean elevations above 3000 m and extremely complex terrain characterized by high mountains and deep valleys, whereas the eastern part is the Sichuan Basin, with elevations of only about 400–1000 m and relatively flat, open terrain. The steep relief of the Tibetan Plateau and the Hengduan Mountains, together with the sharp topographic gradient between the plateau and the basin, provides an important dynamical and thermal background for SWV formation. The study region is located in a transition zone between the East Asian monsoon region and the plateau climate. In the warm season, monsoonal moisture transport converges over the Sichuan Basin and surrounding areas and interacts with downslope flows from the plateau, shear lines, and low-level jets, providing favorable thermodynamic and moisture conditions for SWV development and associated hazardous rainfall.

2.2. Datasets

This study makes use of three primary datasets: the GPM/DPR product spanning 2014–2022, contemporaneous observations from the geostationary meteorological satellites FY-2E and FY-2G, and the Southwest Vortex Yearbook. A brief description of each dataset is provided below.

2.2.1. Satellite Datasets

The GPM/DPR 2A-DPR-FS product (Version 07) is used to characterize the vertical structure and macro- and microphysical properties of SWV precipitation. As the successor to the TRMM satellite, the GPM provides improved spatial coverage and higher measurement accuracy, with an enhanced capability for detecting light precipitation and solid precipitation [39,40]. The DPR onboard the GPM is a dual-frequency precipitation radar system composed of a Ku-band channel (13.6 GHz) and a Ka-band channel (35.5 GHz). By exploiting frequency-dependent scattering differences between the two channels, DPR provides more reliable retrievals of precipitation microphysical parameters than traditional single-frequency radars. The DPR variables used include the radar reflectivity factor Z_e (dBZ), precipitation type, the intercept parameter of raindrop number concentration dBN_w (=10 $\times$ $\log_{10}$ N_w, mm^{-1} m^{-3}), mass-weighted mean diameter D_m (mm), rainfall rate R (mm h^{-1}), near-surface rainfall rate R_s (mm h^{-1}), rain echo top height H_{ET} (m), and freezing-level height T_0 (°C). The horizontal and vertical detection ranges of DPR are approximately 250 km and 22 km, respectively, with corresponding horizontal and vertical resolutions of about 5 km and 250 m. Numerous studies have evaluated and validated the GPM/DPR products [41–47]. For the Sichuan region, Li et al. (2026) conducted a comparison between S-band ground-based weather radar and GPM/DPR data and reported a mean reflectivity error of only 0.18 dBZ [48]. Li et al. (2022) [49] used a network of ground-based laser disdrometers to compare the disdrometer observations with near-surface GPM/DPR results and found good consistency between the two datasets, indicating that GPM/DPR observations are reliable over the Sichuan Basin and the surrounding mountainous areas.

Infrared cloud-top information is obtained from the FY-2E and FY-2G geostationary meteorological satellites operated by the China Meteorological Administration. Both satellites are equipped with the Visible and Infrared Spin-Scan Radiometer (VISSR). In this study, the infrared window channel IR1 (10.3–11.3 μm) brightness temperature (TBB) data are used to track cloud evolution and identify the life-cycle stage of SWV precipitation systems. The native nadir spatial resolution of the IR1 channel is approximately 5 km, while the operational hourly averaged product employed here has an effective spatial resolution of about 10 km. FY-2E was operational from 2009 to 2014, and FY-2G from 2015 to 2022, providing continuous geostationary infrared observations over the study period.

2.2.2. Southwest Vortex Yearbook

The Southwest Vortex Yearbook is compiled and published by the Chengdu Institute of Plateau Meteorology, China Meteorological Administration, in collaboration with the Plateau Meteorology Committee of the Chinese Meteorological Society. The Yearbook is an official operational dataset that systematically documents SWV activity over southwestern China using a combination of enhanced upper-air soundings, satellite imagery, surface meteorological observations, and weather radar data. For each SWV event, the Yearbook provides detailed information including the event identifier, genesis time and location, source region, duration, movement path, intensity evolution, and associated precipitation impacts, such as affected areas, precipitation days, and accumulated rainfall. A weather system is identified as a SWV when it simultaneously satisfies the following criteria [50]:

(1) A vortex evident at the 700-hPa level that forms over the lee side of the Tibetan Plateau (99–109°E, 26–33°N);
(2) The vortex appears on synoptic charts in at least two consecutive analyses, or appears only once but is accompanied by a distinct cloud vortex;
(3) The system has either a closed low with closed height contours or a vortical circulation with cyclonic winds observed at three surrounding stations.

2.3. Selection of SWV Cases Observed by GPM/DPR Overpasses

To analyze the vertical structure and macro- and microphysical characteristics of SWV precipitation over Sichuan using GPM/DPR measurements, we first identify and screen all SWV events during the study period. Although a number of objective SWV identification schemes based on wind fields and geopotential height fields have been proposed [5,51–53], these methods rely on reanalysis datasets, whose representation of lower-tropospheric atmospheric fields over western Sichuan and the eastern Tibetan Plateau with complex terrain remains subject to considerable uncertainties. In view of this, the present study adopts the Southwest Vortex Yearbook, which is widely used in China's operational and research meteorological communities. After compiling all yearbook-identified SWV events, we perform a spatiotemporal collocation with GPM/DPR overpass times and retain only those samples for which an SWV is located over Sichuan Province at the overpass time. To ensure that selected events are associated with substantial rainfall, we further restrict the analysis to cases in which the cloud-precipitation system sampled by DPR has a horizontal area greater than 100 km^2. According to these criteria, a total of 64 SWV precipitation events are obtained, and their occurrence dates together with the corresponding DPR overpass times are listed in Table 1. It shows that most SWV precipitation events are sampled only once by DPR, and only 10 events are observed twice during their life cycles.

Table 1. The selected SWV cases and corresponding DPR overpass times.

Case Number	Date of the SWV Case	Overpass Time of GPM/DPR	Case Number	Date of the SWV Case	Overpass Time of GPM/DPR
1	2014/03/31–04/01	2014/03/31~12:06	34	2019/07/30	2019/07/30~09:03
2	2014/06/19–06/20	2014/06/19~12:48	35	2019/09/16–09/17	2019/09/16~18:49
3	2014/07/02–07/07	2014/07/02~22:46 2014/07/03~08:30	36 37	2020/04/06–04/07 2020/05/20–05/21	2020/04/07~17:09 2020/05/20~18:19
4	2014/08/01–08/03	2014/08/01~00:30	38	2020/06/13–06/14	2020/06/13~21:27
5	2014/08/20–08/23	2014/08/22~17:56	39	2020/06/26–06/28	2020/06/27~07:25
6	2014/08/26–08/27	2014/08/27~16:44			2020/06/27~17:09
7	2014/09/12–09/15	2014/09/13~11:18	40	2020/06/29–07/02	2020/06/29~16:58
8	2015/04/30–05/01	2015/05/01~06:24	41	2020/07/05–07/09	2020/07/05~14:54
9	2015/06/05–06/07	2015/06/07~19:20	42	2020/07/10–07/16	2020/07/16~01:53
10	2015/07/08–07/09	2015/07/09~10:20	43	2020/08/11–08/12	2020/08/11~18:16
11	2015/07/13–07/17	2015/07/14~09:05 2015/07/14~18:49			2020/08/12~04:00
			44	2020/08/16–08/19	2020/08/17~02:48
12	2015/08/15–08/20	2015/08/16~09:02	45	2020/08/30–08/31	2020/08/30~12:44
13	2015/08/26–08/29	2015/08/27~05:42	46	2021/06/16–06/17	2021/06/16~00:00
14	2015/09/05–09/06	2015/09/06~03:20			2021/06/16~09:44
15	2016/03/22–03/24	2016/03/23~16:39	47	2021/06/26	2021/06/26~20:43
16	2016/04/13–04/14	2016/04/14~00:25	48	2021/06/27–07/03	2021/06/28~20:31
17	2016/04/21–04/23	2016/04/22~07:56	49	2021/07/09–07/13	2021/07/09~17:11
18	2016/06/21–06/22	2016/06/22~14:13	50	2021/07/14–07/18	2021/07/14~15:57
19	2016/07/05–07/06	2016/07/06~00:11			2021/07/15~15:06

Table 1. *Cont.*

Case Number	Date of the SWV Case	Overpass Time of GPM/DPR	Case Number	Date of the SWV Case	Overpass Time of GPM/DPR
20	2016/07/13–07/14	2016/07/13~21:56	51	2021/08/16–08/17	2021/08/16~16:01
21	2016/07/21–07/22	2016/07/22~05:29	52	2021/08/22–08/23	2021/08/22~04:12
22	2016/09/18–09/19	2016/09/19~02:18			2021/08/22~13:56
23	2017/04/24–04/26	2017/04/24~20:28	53	2021/09/04–09/05	2021/09/04~00:47
24	2017/06/03–06/05	2017/06/03~22:48			2021/09/04~10:31
		2017/06/04~08:32	54	2021/09/04–09/05	2021/09/05~09:40
25	2017/07/06–07/09	2017/07/08~22:35	55	2022/03/04–03/05	2022/03/05~19:13
26	2018/03/18	2018/03/18~20:26	56	2022/03/21	2022/03/21~14:38
27	2018/04/23–04/25	2018/04/24~23:46	57	2022/04/14–04/15	2022/04/14~17:33
28	2018/05/05–05/06	2018/05/05~20:27	58	2022/05/09–05/10	2022/05/10~23:53
29	2018/07/02–07/06	2018/07/04~03:09	59	2022/05/13–05/14	2022/05/13~22:50
30	2019/06/25	2019/06/25~05:31	60	2022/05/26–05/28	2022/05/26~19:12
31	2019/07/11–07/12	2019/07/11~14:31	61	2022/05/29–05/31	2022/05/31~17:55
		2019/07/12~00:15	62	2022/06/16–06/19	2022/06/16~13:13
32	2019/07/18–07/21	2019/07/19~12:17	63	2022/07/17–07/21	2022/07/18~13:49
		2019/07/19~22:02	64	2022/09/20	2022/09/20~09:12
33	2019/07/22	2019/07/22~11:17			

2.4. Classification of SWV Life-Cycle Stages and Precipitation Types

Following previous studies [31,34,54–57], we further classify SWV precipitation sampled by GPM/DPR into different life-cycle stages based on the temporal evolution of TBB from the FY-2E/FY-2G satellites. Specifically, the developing stage is defined as the period when TBB decreases persistently while the cloud-cluster area increases; the mature stage as the period when TBB is near its minimum and remains nearly unchanged over adjacent times; and the dissipating stage as the period when TBB increases while the cloud-cluster area decreases.

Figure 2 provides examples illustrating how SWV precipitation is classified into the three life-cycle stages. The first-column panels show the composite reflectivity factor (defined as the maximum radar reflectivity over all height levels) at the GPM/DPR overpass time, and the second- to fourth-column panels show the satellite TBB fields at adjacent times before and after the overpass. In the first row of Figure 2, the TBB at 0500 and 0600 UTC (Coordinated Universal Time) is generally higher than that at 0700 UTC, and the low-TBB cloud-cluster area is smaller; therefore, the case at the GPM/DPR overpass time is classified as developing. In the second row, TBB remains below 190 K both before and after the overpass and the cloud-cluster area is largest, so the case is classified as mature. In the third row, around the overpass time (1100 UTC), the cloud-cluster area gradually decreases while TBB increases, indicating a typical dissipating-stage event.

GPM/DPR products categorize the observed precipitation into three types: stratiform precipitation, convective precipitation, and other precipitation. A number of studies have also proposed more refined classification schemes. For example, Huo et al. (2019) [58] classified precipitation into four types: stratiform, convective, mixed, and shallow, using a C-band continuous-wave vertical-pointing precipitation radar. Huang et al. (2016) [59] divided precipitation into five categories based on wind-profiler radar observations: shallow convection, shallow stratiform, deep convection, deep stratiform, and a mixed type. Fu et al. (2008) [60] classified precipitation over the Tibetan Plateau into three types using TRMM/PR observations: deep strong convective, deep weak convective, and shallow convective. For the Sichuan region, Li et al. (2022) [49] further subdivided GPM/DPR precipitation into stratiform precipitation, deep strong convective precipitation, deep weak convective precipitation, and shallow precipitation.

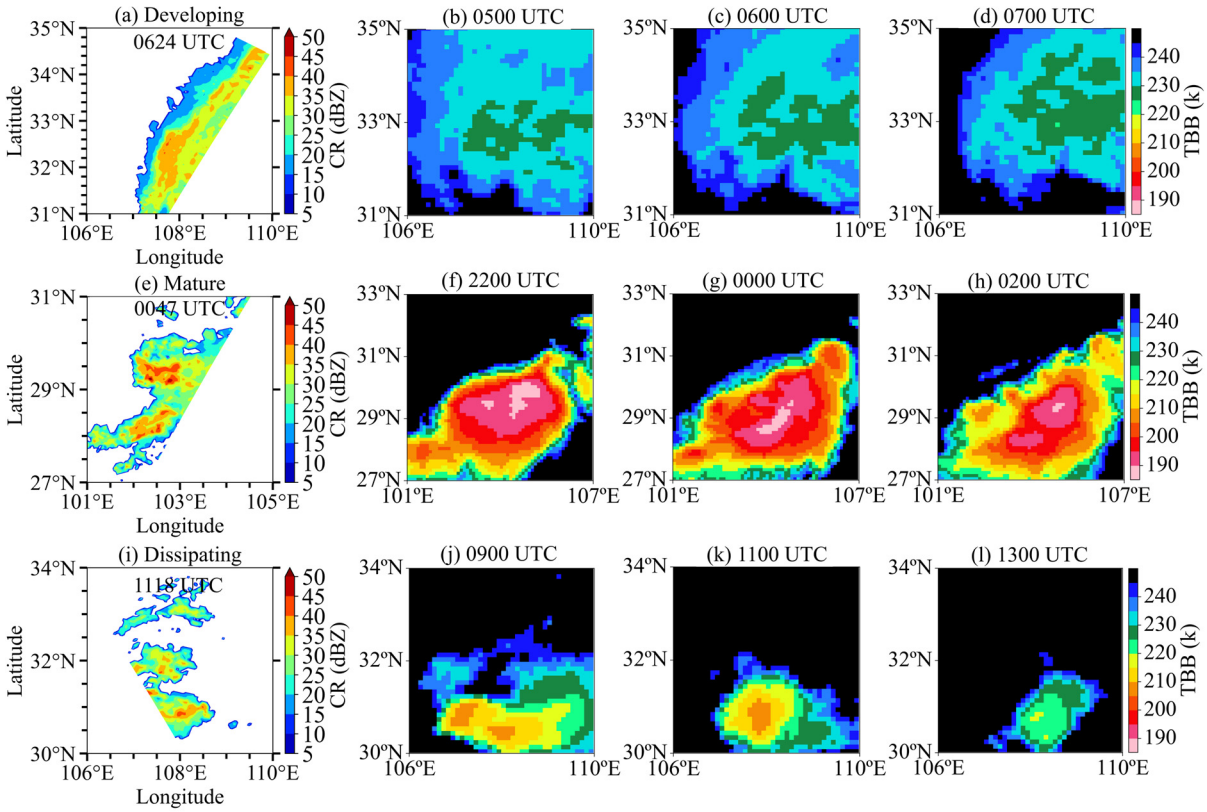

Figure 2. Examples of identifying SWV precipitation in the developing, mature, and dissipating stages. The first column shows the composite reflectivity factor (CR, dBZ) observed by GPM/DPR, and the second to fourth columns show the brightness temperature (TBB) distributions at times before and after the GPM/DPR overpass.

In this study, following Li et al. (2022) [49], we reclassify SWV precipitation sampled during GPM/DPR overpasses by combining the DPR precipitation type, bright-band information, and echo-top height. The classification rules are as follows:

(1) DPR-identified stratiform precipitation with a bright band is defined as stratiform precipitation (STRA);
(2) DPR-identified stratiform precipitation without a bright band, with echo-top height exceeding 7.5 km and reflectivity below 39 dBZ, is defined as deep weak convective precipitation (DWC);
(3) DPR-identified convective precipitation with echo-top height exceeding 7.5 km is defined as deep strong convective precipitation (DSC);
(4) DPR-identified convective precipitation with echo-top height below the 0 °C level is defined as shallow precipitation (SHAL).

Note that the thresholds of 7.5 km echo-top height and 39 dBZ reflectivity factor are physically motivated. The 39 dBZ criterion is consistent with the DPR definition of convective precipitation, while the 7.5 km echo-top height corresponds to a transition in the vertical reflectivity profile slope identified over the Tibetan Plateau, separating deep and shallow precipitation regimes [60]. This combined threshold approach helps reduce the known overclassification of stratiform precipitation by the DPR algorithm over complex terrain and is therefore suitable for characterizing SWV precipitation over our study region.

Figure 3 presents an example of precipitation-type classification for an SWV event on 11 August 2020. Figure 3a,b show the composite reflectivity factor and echo-top height detected at the GPM/DPR overpass time, respectively. Figure 3c illustrates the vertical profile of radar reflectivity extracted along the black solid line in Figure 3a. Figure 3d–f

compare the classification results from the method used in this study with those from the official DPR precipitation classification and the method of Fu et al. (2008) [60]. Along the cross-section, three precipitation types are mainly identified: regions with strong reflectivity and a deep vertical extent correspond to DSC precipitation; regions with relatively weaker reflectivity but still high echo-top heights correspond to DWC precipitation; and regions with weaker reflectivity accompanied by an evident bright band correspond to STRA precipitation. Comparisons among the different schemes indicate that the original DPR classification does not distinguish DWC precipitation and therefore tends to overestimate STRA precipitation, whereas the method of Fu et al. (2008) [60] tends to overestimate DWC precipitation and underestimate (or neglect) STRA precipitation. In contrast, the method used in this study yields a more physically consistent partitioning for SWV precipitation over complex terrain.

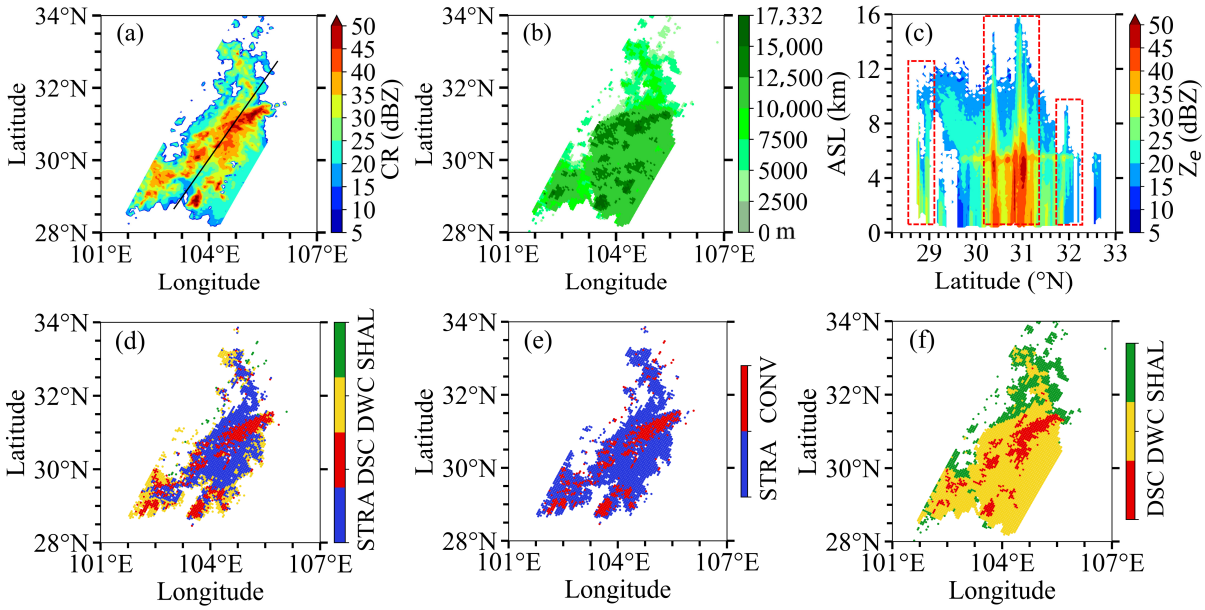

Figure 3. Example of precipitation-type classification for an SWV event on 11 August 2020. Panels (**a**,**b**) show the GPM/DPR composite reflectivity factor and echo-top height, respectively. Panel (**c**) shows the vertical profile of radar reflectivity extracted along the black solid line in (**a**). Panels (**d**–**f**) compare the classification results from the method used in this study with those from the official GPM/DPR classification and the method of Fu et al. (2008) [60]. In subfigure (**c**), the red dashed rectangles denote three regions with different precipitation types.

3. Results

3.1. Characteristics and Differences of SWV Precipitation Across Life-Cycle Stages

To quantify stage-dependent contrasts in SWV precipitation, we first identify all SWV precipitation events sampled during GPM/DPR overpasses. The numbers of valid DPR precipitation profiles for the developing, mature, and dissipating stages are 31,351, 60,747, and 55,856, respectively. Subsequently, we perform statistical analyses of key DPR-derived macroscopic and microphysical variables and compare them among the three stages.

Figure 4 shows violin plots of rain echo-top height (H_{ET}), maximum reflectivity factor in the vertical profile (Z_{max}), maximum height of strong echoes (H_{30}; defined as the highest altitude where $Z_e > 30$ dBZ), and near-surface rainfall rate (R_s) for the three life-cycle stages. Corresponding descriptive statistics, including percentiles, mean, standard deviation, and skewness, are summarized in Table 2. Overall, all four macroscopic variables peak in the mature stage, are intermediate in the dissipating stage, and are smallest in the develop-

ing stage, indicating the strongest storm depth, echo intensity, and near-surface rainfall during maturity.

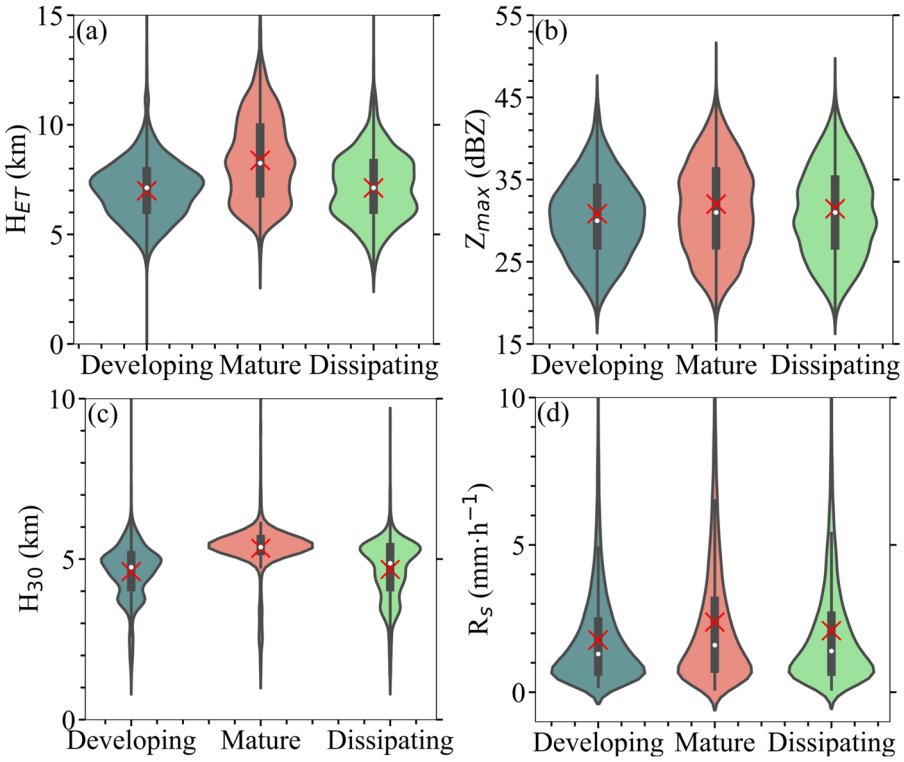

Figure 4. Violin plots of rain echo-top height H_{ET} (**a**), maximum reflectivity factor in the vertical profile Z_{max} (**b**), maximum height of strong echoes H_{30} (Z_e > 30 dBZ) (**c**), and near-surface rainfall rate R_s (**d**) for the developing, mature, and dissipating stages of SWV precipitation. The width of each violin represents the probability density distribution of the corresponding variable. The embedded box indicates the interquartile range (25th–75th percentiles), with the white circles inside the box denoting the median values. The red crosses denote the mean values.

Table 2. Descriptive statistics of the four macroscopic variables for the three life-cycle stages. P5, P25, P50, P75, and P95 denote the 5th, 25th, median, 75th, and 95th percentiles, respectively. Std and Sk are standard deviation and skewness, respectively.

Radar Variables	Life-Cycle Stages	Descriptive Statistics							
		P5	P25	Mean	P50	P75	P95	Std	Sk
H_{ET} (km)	developing	5.0	6.1	7.0	7.1	7.9	9.1	1.3	0.4
	mature	5.6	6.9	8.4	8.3	9.9	11.6	1.9	0.4
	dissipating	4.9	6.1	7.1	7.1	8.3	9.6	1.5	0.2
Z_{max} (dBZ)	developing	22.9	27.0	30.9	30.1	34.1	38.3	4.8	0.1
	mature	23.2	27.3	32.0	31.2	36.2	40.3	5.5	0.0
	dissipating	22.1	27.0	31.5	31.1	35.1	40.1	5.4	0.1
H_{30} (km)	developing	3.1	4.1	4.6	4.8	5.1	5.8	0.9	−0.3
	mature	3.5	5.3	5.3	5.4	5.6	6.0	0.8	−0.2
	dissipating	3.1	4.1	4.7	4.9	5.4	5.8	0.9	−0.7
R_s (mm h^{-1})	developing	0.3	0.7	1.8	1.3	2.4	5.0	1.8	3.4
	mature	0.3	0.8	2.4	1.6	3.1	6.9	2.7	4.4
	dissipating	0.3	0.7	2.1	1.4	2.6	5.7	3.1	2.6

Specifically, the 5th–95th percentile ranges of H_{ET} are 5.0–9.1 km, 5.6–11.6 km, and 4.9–9.6 km for the developing, mature, and dissipating stages, respectively, with

mean values of 7.0 km, 8.4 km, and 7.1 km. For Z_{max}, the corresponding ranges are 22.9–38.3 dBZ, 23.2–40.3 dBZ, and 22.1–40.1 dBZ, with mean values of 30.9 dBZ, 32.0 dBZ, and 31.5 dBZ, respectively. The fractions of profiles with Z_{max} > 40 dBZ are 4.78%, 11.57%, and 8.97% for the developing, mature, and dissipating stages, respectively. The strong-echo core is located at higher altitudes during the mature stage than during the other two stages: H_{30} is mainly distributed between 3.5 and 6.0 km with a mean value of 5.3 km, whereas the dissipating and developing stages exhibit lower and more dispersed H_{30} distributions, with main ranges of 3.1–5.8 km and 3.0–5.8 km and mean values of 4.6 km and 4.7 km, respectively.

Stage-dependent contrasts are also evident in R_s. As expected, the mature stage produces more frequent intense near-surface rainfall due to the most vigorous precipitation development and the strongest radar echoes, followed by the dissipating stage, while rainfall near the ground during the developing stage is generally weaker. Similar life-cycle-dependent differences have also been documented in other regions [34,35]. These storm-scale contrasts provide a structural baseline; we next examine how the vertical evolution of Z_e, D_m, and $\mathrm{dB}N_w$ differs across stages to interpret the underlying microphysical pathways (Figure 5).

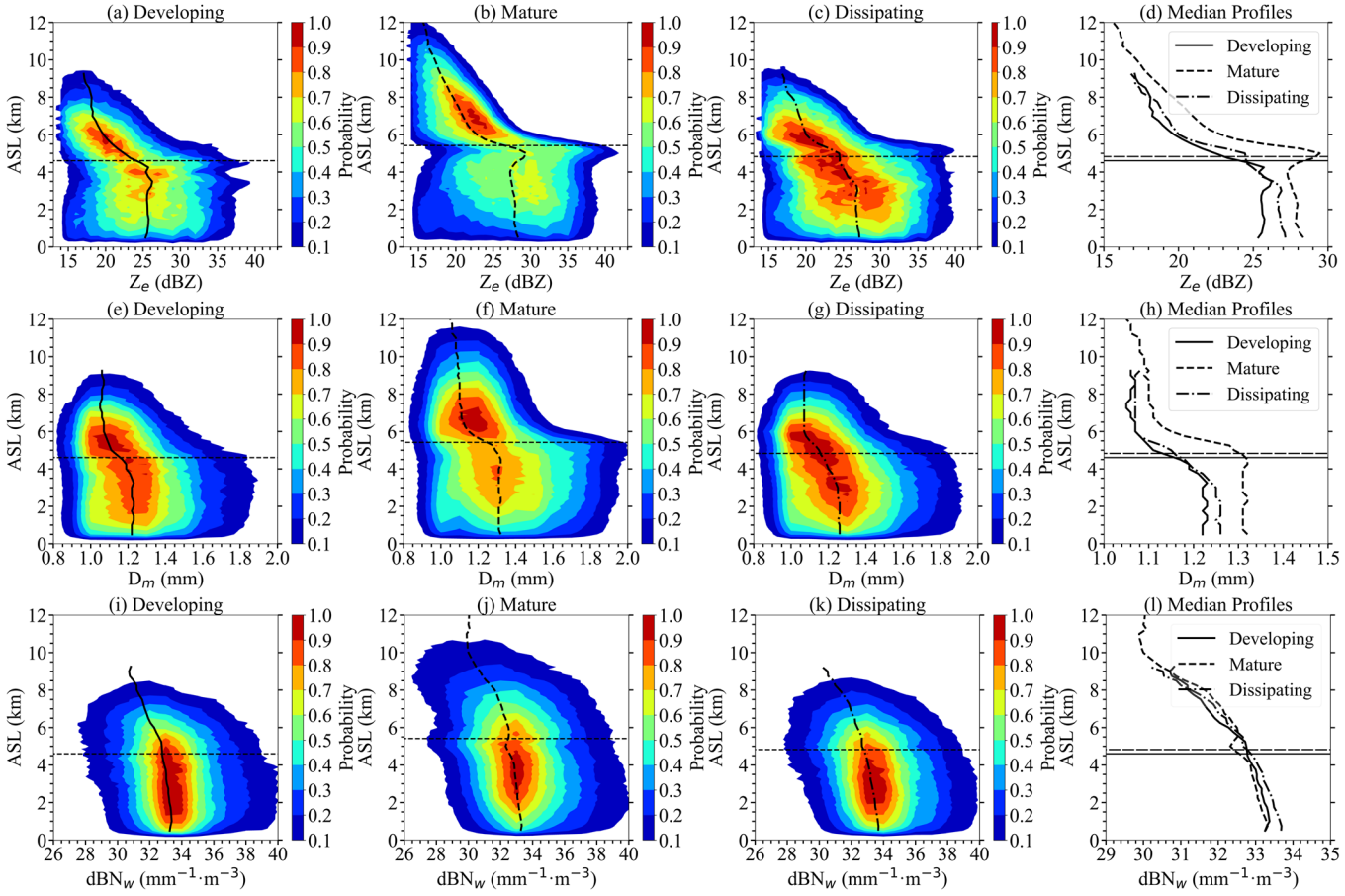

Figure 5. Normalized probability distributions of Z_e (**a**–**d**), D_m (**e**–**h**), and $\mathrm{dB}N_w$ (**i**–**l**) as a function of height for the developing (first column), mature (second column), and dissipating (third column) stages. The corresponding median profiles for each variable and stage are shown in the fourth column. The mean 0 °C level for each stage is superimposed as a horizontal black line.

Based on the radar profiles in the three stages, Figure 5 shows the normalized height-dependent probability distributions of Z_e, D_m, and $\mathrm{dB}N_w$, together with the corresponding median profiles. The mean 0 °C level for each stage is superimposed as a horizontal black

line. Consistent with the macroscopic metrics in Figure 4, the mature stage features deeper and broader height-dependent distributions of Z_e, D_m, and $\mathrm{dB}N_w$, whereas the dissipating stage is intermediate and the developing stage is the weakest. The mean 0 °C level is also higher in the mature stage, while the developing and dissipating stages are comparable, suggesting a generally warmer thermodynamic environment during the mature stage.

Further examination of the median profiles by separating the column into three height intervals reveals the following features. (1) Above the 0 °C level (from echo top down to the freezing level/melting level), Z_e, D_m, and $\mathrm{dB}N_w$ generally increase with decreasing height in all three stages, with higher median values and steeper vertical gradients in the mature stage. This behavior implies more vigorous ice-phase growth during the mature stage, potentially involving stronger aggregation and riming, with the dissipating stage intermediate and the developing stage relatively weak. (2) Near the 0 °C level and within the melting layer, the mature stage exhibits a more evident bright-band signature (a more prominent peak of Z_e around the 0 °C level), together with a larger increase in D_m and a stronger decrease in $\mathrm{dB}N_w$ below the melting layer. This coupled evolution indicates a stronger post-melting shift of the raindrop size distribution toward larger drops and lower number concentrations, consistent with more efficient collision–coalescence growth and/or size sorting [61–64]. (3) In the warm-rain region, the vertical variations become weaker; Z_e and D_m remain the largest while $\mathrm{dB}N_w$ is the smallest in the mature stage, and the three variables in the dissipating stage are slightly larger than those in the developing stage. Notably, near the surface, the median profiles of Z_e and $\mathrm{dB}N_w$ decrease in the developing stage, whereas D_m shows little change. This pattern may reflect evaporation preferentially reducing small drops in the near-surface layer, lowering number concentration and reflectivity while exerting a relatively limited influence on D_m. In contrast, during the mature stage, Z_e and D_m continue to increase toward the surface with a slightly decrease in $\mathrm{dB}N_w$, suggesting that warm-rain growth and spectral evolution dominate under moister conditions and stronger precipitation. Overall, SWV precipitation exhibits distinct vertical structures and macro- and microphysical evolution pathways across different life-cycle stages.

Motivated by the below-melting-layer evolution in Figure 5, we further diagnose dominant warm-rain processes using the differential metrics ΔZ_e and ΔD_m between 3 km and 1 km, following Kumjian and Prat (2014) [65] and Wen et al. (2023) [66]. Specifically, $\Delta Z_e = Z_e(1\ \mathrm{km}) - Z_e(3\ \mathrm{km})$ and $\Delta D_m = D_m(1\ \mathrm{km}) - D_m(3\ \mathrm{km})$. These two differential metrics capture the combined effects of changes in radar reflectivity and characteristic drop size during descent through the lower troposphere, providing insight into the dominant warm-rain microphysical processes.

Figure 6a–c show the ΔZ_e–ΔD_m distributions and the corresponding proportions for the developing, mature, and dissipating stages, respectively, and Figure 6d schematically summarizes the dominant processes associated with the four quadrants. Specifically, when ΔZ_e and ΔD_m are both positive (both negative), collision–coalescence growth (drop breakup) is inferred to dominate. When $\Delta Z_e > 0$ but $\Delta D_m < 0$, a balance between coalescence and breakup is suggested, which can increase reflectivity while reducing characteristic drop size. When $\Delta Z_e < 0$ but $\Delta D_m > 0$, evaporation-related processes that preferentially reduce number concentration are inferred to be more pronounced, yielding weaker reflectivity but relatively larger D_m. Overall, breakup and the coalescence-breakup balance dominate across all three stages, but notable stage-dependent differences are evident: the mature stage shows the largest fraction of coalescence-dominated samples, whereas the dissipating stage exhibits relatively higher proportions of breakup and evaporation, and the developing stage is characterized by the largest percentage of the coalescence-breakup balance regime. These process-level differences provide a mechanistic explanation

for the stage-dependent low-level evolution of the raindrop size distribution inferred from Figure 5.

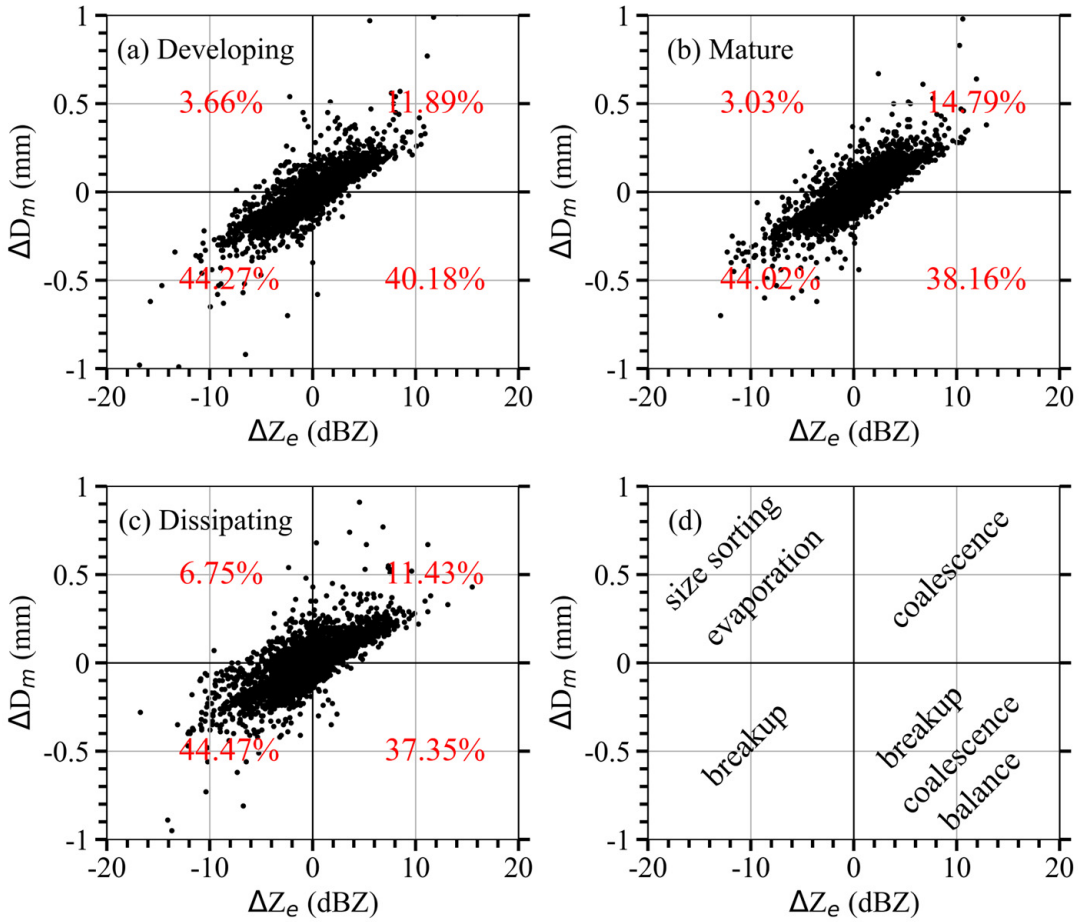

Figure 6. The ΔZ_e–ΔD_m distribution patterns and corresponding proportions for all samples in the developing (**a**), mature (**b**), and dissipating (**c**) stages, and a schematic summary of dominant microphysical processes for the four quadrants (**d**).

3.2. Characteristics and Differences Among SWV Precipitation Types

For all SWV precipitation events, the total number of DPR profiles (and corresponding proportions) classified as STRA, DSC, DWC, and SHAL are 44,600 (46.3%), 15,352 (16%), 34,883 (36.3%), and 1392 (1.4%), respectively. The results show that SWV precipitation over Sichuan is dominated by STRA and DWC in terms of sample counts. To further quantify differences in vertical structure and macro-and microphysical characteristics among the four precipitation types, we next conduct a statistical comparison of DPR-derived variables among the different precipitation types.

Figure 7 compares the macroscopic parameters of H_{ET}, Z_{max}, H_{30}, and R_s among STRA, DSC, DWC, and SHAL, and the corresponding statistics are summarized in Table 3. Overall, DSC exhibits the largest values for all four variables, indicating the deepest vertical development, the strongest radar echoes, and the most intense near-surface precipitation among the four types. STRA and DWC show comparable echo-top heights, whereas STRA generally features stronger echoes (higher $Z_{\max}$ and H_{30}) and larger R_s than DWC, suggesting more robust precipitation development despite similar storm-top heights. SHAL is characterized by significantly lower H_{ET} and H_{30}, together with weaker $Z_{\max}$, reflecting its shallow vertical structure.

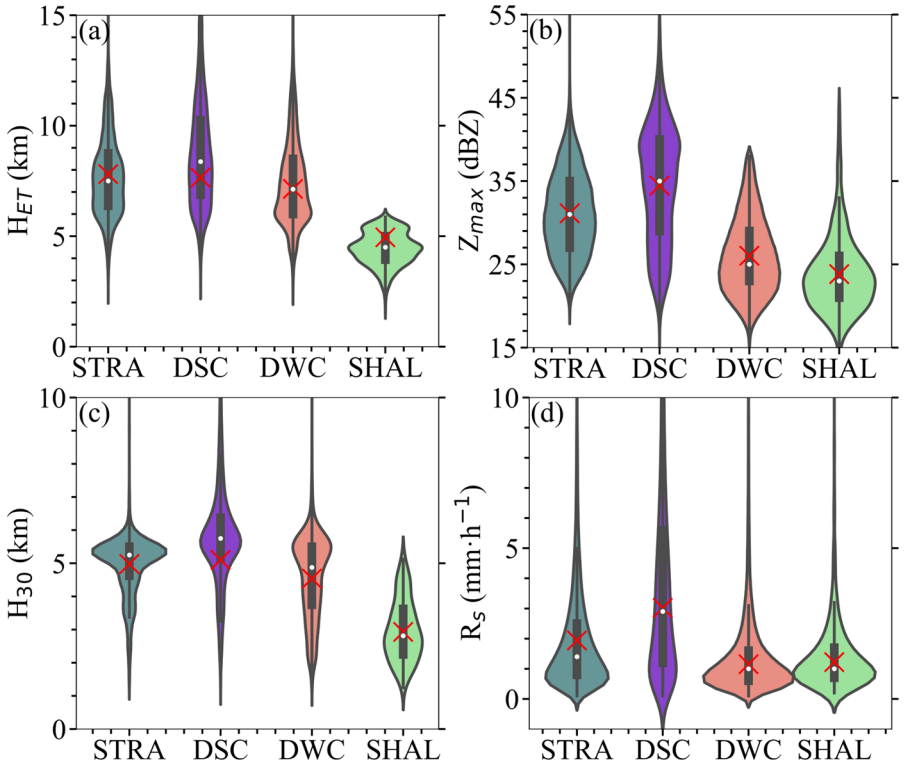

Figure 7. Violin plots of H_{ET} (**a**), Z_{max} (**b**), H_{30} (**c**), and R_s (**d**) for the STRA, DSC, DWC, and SHAL precipitation types. The meaning of each violin is the same as that described in the caption of Figure 4.

Table 3. Descriptive statistics of the four macroscopic variables for the four precipitation types. The abbreviations are the same as in Table 2.

Radar Variables	Precipitation Types	Descriptive Statistics							
		P5	P25	Mean	P50	P75	P95	Std	Sk
H_{ET} (km)	STRA	5.1	6.4	7.8	7.5	8.8	11.0	1.7	0.6
	DSC	5.5	6.9	7.7	8.4	10.3	13.5	1.9	0.7
	DWC	4.8	6.0	7.1	7.1	8.5	11.1	1.9	1.1
	SHAL	3.1	3.9	5.0	4.5	5.0	5.6	0.6	−1.0
Z_{max} (dBZ)	STRA	23.9	27.0	31.1	31.0	35.2	40.2	4.7	0.1
	DSC	23.1	29.1	34.5	35.2	40.0	45.3	6.4	0.2
	DWC	19.0	22.8	26.0	25.2	29.1	35.2	4.3	0.6
	SHAL	18.1	21.2	23.8	23.1	25.8	32.7	3.9	1.6
H_{30} (km)	STRA	3.1	4.6	5.0	5.3	5.5	5.9	0.9	−0.5
	DSC	3.3	5.1	5.1	5.8	6.4	8.8	1.1	0.0
	DWC	2.3	3.8	4.5	4.9	5.5	6.1	1.4	−0.4
	SHAL	1.8	2.3	2.9	2.8	3.6	4.6	0.9	0.4
R_s (mm h^{-1})	STRA	0.4	0.8	1.9	1.4	2.5	5.6	1.8	4.6
	DSC	0.4	1.2	3.0	2.9	5.6	13.0	4.3	6.7
	DWC	0.3	0.6	1.2	1.0	1.6	4.0	1.2	2.7
	SHAL	0.4	1.7	1.2	1.0	1.7	3.6	1.1	2.7

Figure 8 shows the normalized height-dependent probability distributions of Z_e, D_m, and dBN_w for the four precipitation types, in the same format as Figure 5. The first four columns correspond to DSC, STRA, DWC, and SHAL, respectively, and the fifth column summarizes the median profiles. The high-frequency cores (normalized probability > 0.5) provide a compact measure of the typical value ranges and their vertical extents, while the median profiles help diagnose systematic microphysical evolution across the ice-phase

region, the melting layer, and the warm-rain region. For Z_e, the core of DSC extends through a much deeper layer (1.2–10.3 km; $Z_e \approx$ 15.5–42 dBZ), STRA and DWC fall in between with narrower cores, whereas SHAL is largely confined to 0.6–4.5 km with substantially weaker echoes ($Z_e \approx$ 15–26.1 dBZ). Consistent signals are also evident in D_m and dBN_w: DSC tends to have larger characteristic sizes (D_m) over a deeper layer, whereas SHAL exhibits smaller D_m but substantially larger dBN_w, indicative of a population dominated by more numerous small drops. Together, these structural differences indicate systematic contrasts among the four precipitation types in vertical development depth, radar echo intensity, and drop-size structure.

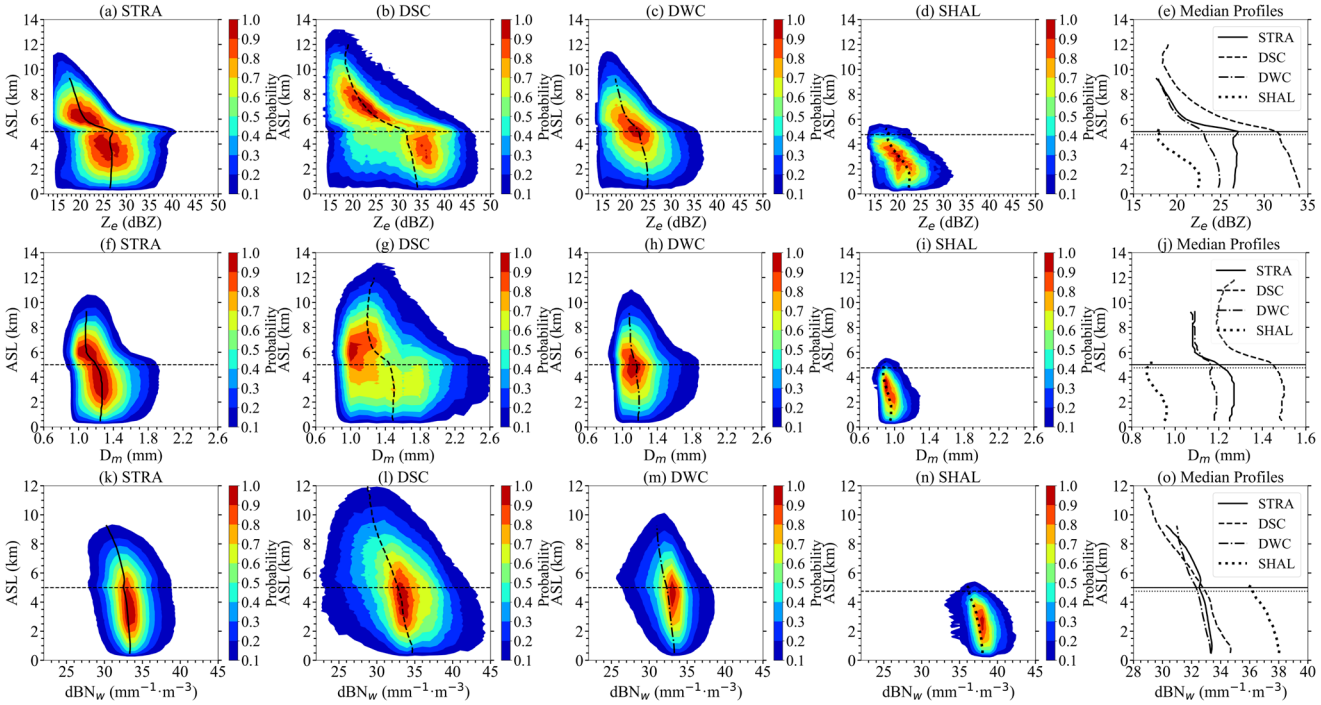

Figure 8. Normalized probability distributions of Z_e (**a–e**), D_m (**f–j**), and dBN_w (**k–o**) as a function of height for the STRA (first column), DSC (second column), DWC (third column), and SHAL (fourth column) precipitation types. The corresponding median profiles for each variable and precipitation type are shown in the fifth column. The mean 0 °C level for each precipitation type is superimposed as a horizontal black line.

Further analysis of the median profiles highlights distinct characteristics and differences among the four precipitation types within three phase-related height intervals. (1) Above the 0 °C level (from echo top down to the freezing/melting level), DSC shows larger median values of Z_e and D_m and a stronger increase with decreasing height, suggesting more intense ice-phase particle growth, potentially associated with more active vapor deposition, aggregation, and riming processes. In contrast, STRA and DWC show weaker vertical variations in ice-phase D_m; meanwhile, STRA often features higher dBN_w, suggesting higher number concentrations of smaller ice particles, consistent with steadier stratiform ascent and sustained moisture supply. (2) Near the melting layer, STRA displays the most distinct and strongest bright-band structure, whereas the bright-band signatures in DSC and DWC are relatively weak or less apparent, indicating that their vertical structures are more strongly modulated by convective updrafts, turbulence, and mixed-phase hydrometeors. (3) In the warm-rain region, DSC maintains the largest Z_e and D_m, consistent with the most active liquid-phase growth, while STRA and DWC weaken sequentially. SHAL is characterized by the smallest Z_e and D_m but considerably higher dBN_w, indicating precipitation dominated by a high concentration of small drops. Notably, D_m in SHAL

increases relatively rapidly toward lower altitudes, likely reflecting the combined effects of warm-rain collision–coalescence growth and spectral sorting during descent.

Figure 9 illustrates the ΔZ_e–ΔD_m distributions for the four precipitation types within the 1–3 km liquid-phase layer, together with the fractional contributions in the four quadrants; the dominant warm-rain microphysical process associated with each quadrant is also indicated. The results show that, in the warm-rain layer for all four types, samples attributed to coalescence and breakup account for substantially larger proportions than those associated with evaporation-size sorting and the coalescence–breakup balance. Notable inter-type differences are evident: DSC exhibits a higher contribution from evaporation-size sorting while maintaining a strong coalescence process; STRA is characterized by the largest fraction of breakup-dominated samples; the coalescence-breakup balance is most prominent in DWC; and SHAL exhibits the strongest dominance of coalescence.

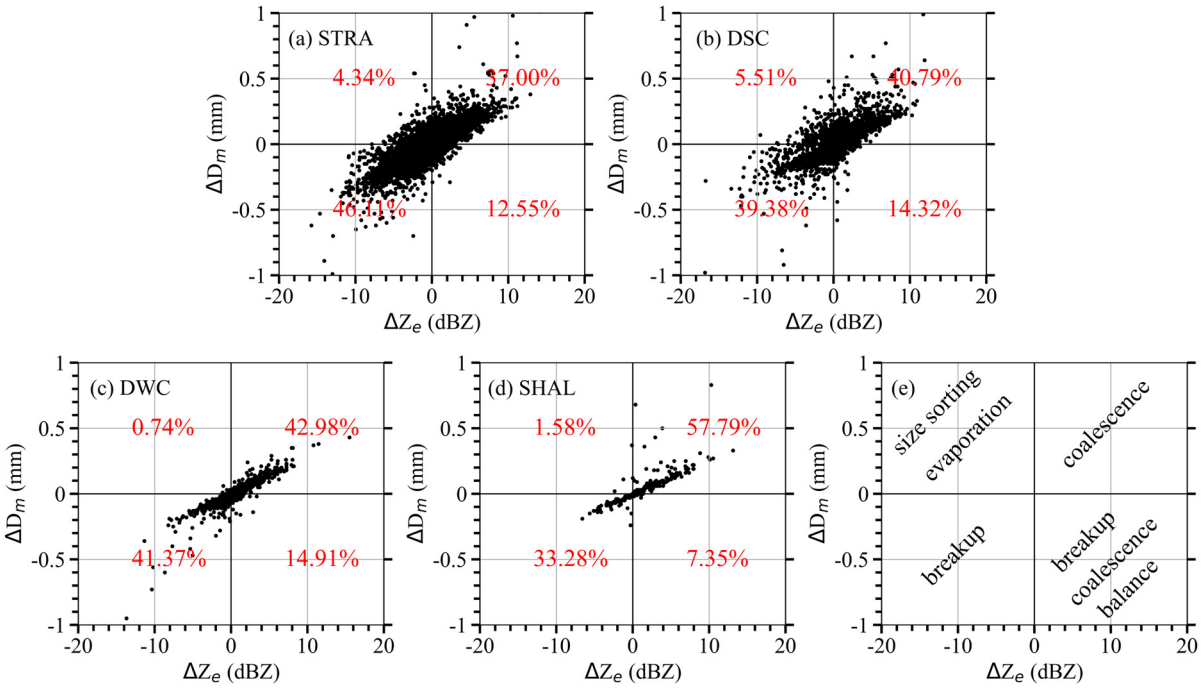

Figure 9. The ΔZ_e–ΔD_m distribution patterns and corresponding proportions for all samples for STRA (**a**), DSC (**b**), DWC (**c**), and SHAL (**d**), and a schematic summary of the dominant microphysical processes (**e**) associated with the four quadrants in the ΔZ_e–ΔD_m plane.

4. Validation, Discussion and Comparison

In this section, we first assess the reliability of the GPM/DPR macro- and microphysical measurements over complex terrain through a preliminary validation against ground-based disdrometer observations. Subsequently, we interpret the stage- and type-dependent characteristics of southwest vortex (SWV) precipitation identified in Sections 3.1 and 3.2 in terms of their underlying physical mechanisms, and place the results in a broader context by comparison with other rainy-season precipitation regimes in China.

4.1. Preliminary Validation of GPR/DPR Observations

To evaluate the reliability of GPM/DPR observations over the complex terrain considered in this study, observations from 15 ground-based PARSIVEL^2 disdrometer stations (as marked by red crosses in Figure 1 and were manufactured by OTT HydroMet, Kempten, Germany) across Sichuan Province during 2019–2022 were used to conduct a preliminary validation of the DPR-measured Z_e, R, D_m, and N_w. After applying space-time collocation between satellite and ground observations, a total of 823 matched precipitation samples

were obtained. The four variables from the DPR near-surface bin were then compared with the corresponding disdrometer observations, as shown in Figure 10. The scatter distributions, correlation coefficients (CC), and mean absolute errors (MAE) indicate generally good agreement between the two observing systems. Specifically, the CC and MAE are 0.81 and 3.89 dB for Z_e, 0.86 and 0.6 mm h^{-1} for R, 0.74 and 0.21 mm for D_m, and 0.72 and 3.75 $mm^{-1} \cdot m^{-3}$ for dBN_w, respectively.

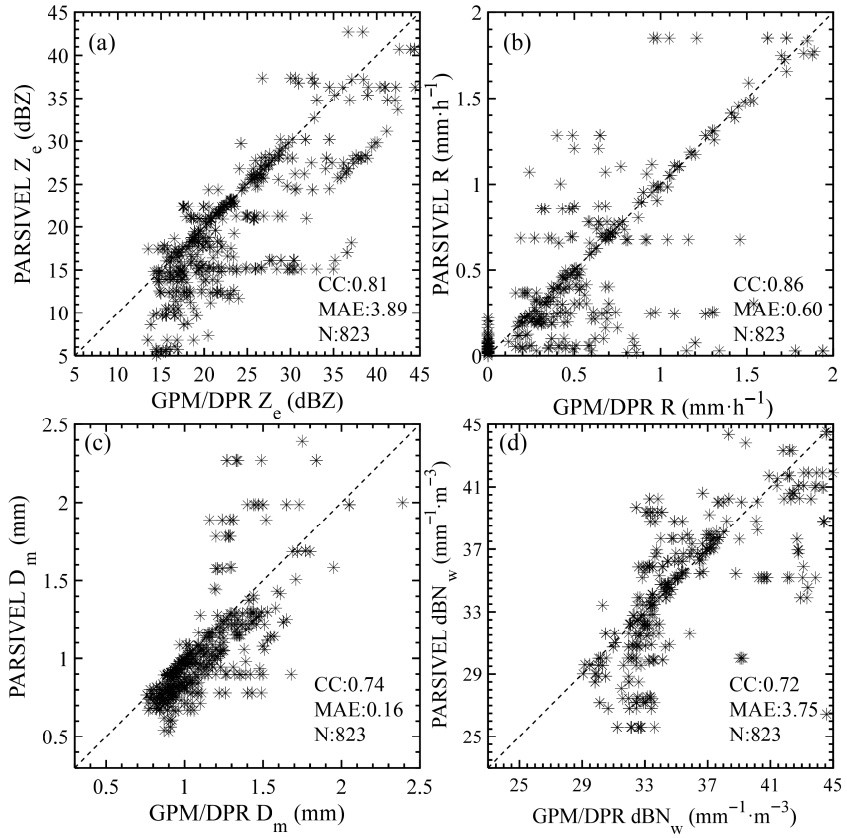

Figure 10. Comparison of Z_e (**a**), R (**b**), D_m (**c**), and N_w (**d**) between GPM/DPR near-surface observations and ground-based PARSIVEL[2] disdrometer measurements. The N, CC, and MAE represent the number of matched samples, correlation coefficient, and mean absolute error, respectively. The asterisks denote samples and the dashed lines represent positions of equal values.

Overall, these results suggest that the GPM/DPR retrievals of the four key macro- and microphysical parameters of SWV precipitation over Sichuan are reasonably reliable. It should be noted, however, that the extremely complex terrain in the study region may influence precipitation characteristics within individual DPR footprints. In addition, discrepancies in sampling volume and measurement principles between spaceborne radar and ground-based disdrometers make it difficult to achieve perfectly matched observational conditions.

4.2. Underlying Physical Mechanisms

The variations in the vertical structure and macro-microphysical characteristics of SWV precipitation with respect to life stage and precipitation type identified in Sections 3.1 and 3.2 reflect the coupled evolution of dynamical forcing, moisture availability, and precipitation organization during the vortex life cycle. Rather than acting independently, life-cycle stage and precipitation type jointly modulate the dominant microphysical processes and resulting precipitation structures.

During the developing stage, SWV precipitation exhibits relatively weak vertical development, lower echo-top heights, and reduced near-surface rain rates. Microphysical parameters indicate smaller D_m accompanied by relatively higher N_w, implying precipitation composed of numerous but comparatively small raindrops. This feature is physically consistent with strong but still organizing updrafts, which efficiently loft small liquid and ice-phase particles while limiting sustained collision-coalescence growth below the melting layer. Similar early-stage microphysical signatures have been widely reported for developing convective systems using satellite observations [34,35,55,56].

As the SWV precipitation evolves into the mature stage, enhanced and persistent upward motion together with maximum moisture supply promote deep convection and efficient hydrometeor growth. This stage is characterized by the highest echo-top heights, strongest reflectivity, and largest near-surface rain rates. Correspondingly, D_m reaches its maximum while N_w decreases, indicating that collision-coalescence becomes the dominant growth mechanism and size sorting of raindrops is highly effective during descent. Pronounced bright-band signatures and vertically layered structures further suggest the combined influence of melting and aggregation processes. These characteristics are consistent with previous studies identifying the mature stage as the period of highest precipitation efficiency and most active microphysical growth [35,56,67].

In the dissipating stage, weakening vertical motion and reduced moisture replenishment suppress convective activity, leading to lower echo tops and diminished precipitation intensity. Microphysical parameters show reduced N_w and D_m values that are smaller than those in the mature stage, indicating a decline in the generation of new hydrometeors. Under these conditions, breakup and evaporation processes become relatively more important, as supported by the ΔZ_e–ΔD_m diagnostics presented in Section 3.1. Similar transitions toward stratiform-dominated precipitation and microphysical decay in late life stages have been documented in regional and global studies [34,68].

From the perspective of precipitation type, convective precipitation dominates during the developing and mature stages and is associated with stronger reflectivity cores, larger raindrop sizes, and pronounced vertical gradients, reflecting active mixed-phase processes and efficient collision-coalescence. In contrast, stratiform precipitation becomes increasingly dominant in the dissipating stage, exhibiting more stable layered structures and clear melting-layer signatures, where melting, aggregation, and subsequent breakup and evaporation play a greater role. Overall, the life cycle of the southwest vortex provides a dynamical framework that modulates precipitation type and microphysical pathways, while complex terrain further influences the observed vertical structures over the Sichuan Basin.

4.3. Comparison with Other Regimes in China

To place the SWV precipitation characteristics in a broader climatological and physical context, we compare our observational results with those reported for other rainy-season precipitation regimes in China. To ensure the comparison as objective and comparable as possible, we primarily reference studies that (1) are also based on GPM/DPR observations, (2) focus on similar seasons or observation periods, and (3) employ precipitation-type classifications that are consistent with ours. Specifically, Wen et al. (2023) [66] classified precipitation over eastern China into multiple types, among which the definitions of STRA and SHAL are consistent with those used in this study; moreover, their summer statistics are temporally close to the main occurrence period of our SWV cases. Li et al. (2024) [69] classified rainy-season precipitation over southern China into four categories: stratiform precipitation with a bright band, stratiform precipitation without a bright band, deep convective precipitation, and shallow precipitation. Among these, “bright-band stratiform”

and "shallow" correspond to STRA and SHAL in our classification, respectively. Their observation period spans April to September, covering most months during which the SWV cases analyzed here occur. Table 4 summarizes a comparison of STRA and SHAL precipitation among Sichuan (SWV samples), eastern China (Wen et al., 2023 [66]), and southern China (Li et al., 2024 [69]). The comparison metrics include the altitude ranges and value ranges associated with the high-frequency core of the height-dependent probability distributions (normalized probability > 0.5), as well as the maximum values of the median profiles. The main findings are as follows:

Table 4. Comparison of STRA and SHAL precipitation among Sichuan (SWV samples), eastern China (Wen et al., 2023 [66]), and southern China (Li et al., 2024 [69]). The "height range" and "value range" correspond to the high-frequency core (normalized probability > 0.5) of the height-dependent probability distributions.

Rain Type	Studies	Region	Radar Variables	Height Range	Metrics Value Range	Maximum Median
Stratiform (STRA)	the present	Sichuan Province	Z_e (dBZ)	1.0–8.6	15.0–34.3	27.1
			D_m (mm)	0.75–8.0	0.9–1.5	1.3
			$\mathrm{dB}N_w$ (mm^{-1} m^{-3})	0.8–6.8	31–35.4	33.4
	Wen et al., 2023 [66]	Eastern China	Z_e (dBZ)	1.0–9.7	16.5–25.5	24.1
			D_m (mm)	0.4–9.3	1.1–1.4	1.15
			$\mathrm{dB}N_w$ (mm^{-1} m^{-3})	0.3–8.5	32–36.5	34
	Li et al., 2024 [69]	Southern China	Z_e (dBZ)	0.8–8.5	15.1–34.1	26.5
Shallow (SHAL)	the present	Sichuan Province	Z_e (dBZ)	0.6–4.6	15.1–26.0	22.7
			D_m (mm)	0.65–4.5	0.84–1.08	0.96
			$\mathrm{dB}N_w$ (mm^{-1} m^{-3})	0.6–4.3	36.4–39.6	38
	Wen et al., 2023 [66]	Eastern China	Z_e (dBZ)	0.3–3.5	16.7–22.7	20.5
			D_m (mm)	0.3–3.6	0.85–1.18	0.95
			$\mathrm{dB}N_w$ (mm^{-1} m^{-3})	0.3–2.8	37.6–39.7	38.2
	Li et al., 2024 [69]	Southern China	Z_e (dBZ)	0.3–3.4	14.2–22.8	20.0

(1) For STRA, the height-dependent distributional tendencies of Z_e, D_m, and $\mathrm{dB}N_w$ are broadly similar across the three regions, but their distributional extents and typical magnitudes differ. Overall, compared with STRA precipitation in eastern and southern China, SWV STRA precipitation over Sichuan exhibits a shallower vertical extent, yet wider value ranges for all three variables. In particular, the high-frequency-core values of Z_e and D_m are larger, whereas $\mathrm{dB}N_w$ is smaller. This suggests that SWV STRA precipitation, although geometrically shallower, tends to produce stronger radar echoes and a drop-size structure characterized by larger drops but lower number concentrations.

(2) For SHAL, SWV samples generally exhibit a higher development height than those in the other two regions, while the inter-regional differences in radar-variable magnitudes are smaller than those for STRA. Relative to eastern and southern China, SWV SHAL precipitation shows slightly larger Z_e and D_m, but slightly smaller $\mathrm{dB}N_w$.

(3) In terms of dominant warm-rain microphysical processes inferred from the ΔZ_e–ΔD_m sample distributions and quadrant fractions within the 1–3 km liquid-phase layer, STRA precipitation in all three regions is primarily dominated by breakup, followed by coalescence, but the relative strengths differ. Specifically, SWV STRA precipitation shows a markedly stronger coalescence signature than STRA precipitation in eastern China (summer) and southern China (rainy season), whereas the latter two exhibit a more apparent breakup signature. For SHAL precipitation, all three regions show coalescence dominance with breakup as secondary, but breakup is relatively more

evident in SWV SHAL precipitation, whereas coalescence is stronger in eastern-China summer and southern-China rainy-season SHAL precipitation.

5. Conclusions

To further improve our understanding of the vertical structure and macro-microphysical behavior of SWV precipitation, this study uses nearly nine years of GPM/DPR observations, together with the Southwest Vortex Yearbook and geostationary-satellite TBB data, to systematically examine SWV precipitation over Sichuan across different life-cycle stages and precipitation types. The main conclusions are summarized as follows.

(1) From the life-cycle perspective, both the vertical development depth and precipitation intensity of SWV precipitation exhibit evident stage dependence. The mature stage shows the largest H_{ET}, Z_{max}, H_{30}, and R_s, indicating the deepest development, strongest echoes, and most intense near-surface rainfall; the dissipating stage is intermediate, and the developing stage is the weakest. Consistent with these macroscopic variables, the mature stage features broader and deeper height-dependent probability distributions of Z_e, D_m, and dBN_w, together with a higher 0 °C level. Median profiles further show that ice-phase particle growth above the 0 °C level is more pronounced during the mature stage, the bright-band structure near the melting layer is clearer, and the layer below 0 °C exhibits a stronger coupled change of increasing D_m and decreasing dBN_w, implying a more evident post-melting shift toward larger drops and lower concentrations. Near the surface, decreases in Z_e and dBN_w accompanied by relatively small changes in D_m during the developing stage suggest preferential evaporation of small drops, whereas the mature stage reflects stronger warm-rain growth and spectral evolution. Diagnostics based on ΔZ_e–ΔD_m between 3 and 1 km further indicate that breakup and the coalescence-breakup balance account for relatively large fractions, while the mature stage has a larger coalescence contribution and the dissipating stage exhibits more prominent evaporation- and breakup-related signatures.

(2) Different precipitation types associated with SWVs also exhibit distinct vertical structures and macro-microphysical characteristics. DSC has the greatest vertical extent, strongest echoes, and largest R_s; its high-frequency core of Z_e extends to higher altitudes, and it is characterized by larger D_m and broader distributions, indicating more active ice-phase growth and mixed-phase processes. STRA and DWC have comparable echo-top heights, but STRA typically shows stronger echoes and higher rainfall rates, suggesting more efficient precipitation growth. SHAL is characterized by the smallest D_m but significantly larger dBN_w, indicating precipitation dominated by numerous small drops with noticeable warm-rain spectral evolution. In terms of warm-rain microphysical processes, coalescence and breakup dominate for all four types; however, DSC shows a larger contribution from evaporation–size sorting, STRA is dominated by breakup, the coalescence–breakup balance is most prominent in DWC, and SHAL exhibits the strongest dominance of coalescence.

(3) Comparisons with results for eastern China summer precipitation and southern China rainy-season precipitation indicate that SWV stratiform precipitation over Sichuan is shallower, yet characterized by larger Z_e and D_m and smaller dBN_w, implying stronger echoes and a drop-size structure with larger but less numerous drops, together with a stronger coalescence signature.

Beyond the specific characteristics of SWV precipitation, the findings of this study have broader implications for satellite-based precipitation retrievals and numerical modeling over complex terrain. The significant variations in vertical structure and microphysical parameters with respect to life stage and precipitation type highlight the limitations of retrieval algorithms that rely on static or regionally uniform assumptions. In particular,

the systematic differences in radar reflectivity profiles, melting-layer characteristics, and warm-rain microphysical processes among different SWV stages and precipitation types suggest that incorporating life-stage information from geostationary satellite observations could improve the interpretation of spaceborne radar signals and reduce uncertainties in near-surface rainfall estimation over mountainous regions. Moreover, the identified contrasts in raindrop size distributions and dominant microphysical processes provide observational constraints for cloud microphysics parameterizations in numerical weather prediction models, especially for representing mixed-phase processes, warm-rain growth, and evaporation under complex terrain forcing. These results underscore the value of the synergistic use of low-Earth-orbit precipitation radars and geostationary satellite observations for improving both satellite quantitative precipitation estimation and model-based prediction of SWV-related rainfall.

Despite the reliability of the statistical results, several limitations should be acknowledged. First, although the GPM/DPR provides valuable vertical information, its sampling of individual SWV events is temporally sparse, and the identification of life stages relies on auxiliary geostationary satellite observations rather than continuous radar sampling. Second, uncertainties remain in interpreting microphysical process diagnostics based solely on radar-derived parameters, as hydrometeor phase transitions, such as melting and mixed-phase interactions, can also influence radar reflectivity and complicate the interpretation of ΔZ_e and ΔD_m. In addition, Ka/Ku-band dual-frequency retrievals over complex terrain may still be affected by beam geometry, attenuation, and pixel-mixing effects, particularly for shallow and stratiform precipitation, which introduces additional uncertainty that warrants further investigation.

Future work should therefore focus on integrating longer-term observations, incorporating ground-based radar and in situ measurements for validation, and exploring joint retrieval frameworks that explicitly account for cloud life-cycle evolution. Further coupling satellite-based observational analyses with high-resolution numerical simulations would also be valuable for clarifying the dynamical and microphysical linkages of SWV precipitation and for improving precipitation representation in complex-terrain environments.

Author Contributions: Conceptualization, J.W.; methodology, J.W.; software, Y.L.; validation, Y.L.; formal analysis, Y.L.; investigation, Y.L.; resources, J.Z.; data curation, J.Z.; writing—original draft preparation, Y.L.; writing—review and editing, J.Z.; visualization, Y.L.; supervision, J.Z.; project administration, H.W.; funding acquisition, H.W. All authors have read and agreed to the published version of the manuscript.

Funding: This research was funded by the National Natural Science Foundation of China, grant number 42575154, and the Open Fund Project of Key Laboratory of Intelligent Meteorological Observation Technology, China Meteorological Administration, grant number ZNGC2024ZD12.

Data Availability Statement: The Global Precipitation Measurement Dual-frequency Precipitation Radar (GPM/DPR) data used in this study are publicly available from the National Aeronautics and Space Administration (NASA) Earthdata portal (https://www.earthdata.nasa.gov/data/catalog/ges-disc-gpm-2adpr-07, accessed on 15 June 2024). The Fengyun-2E and Fengyun-2G geostationary satellite data are publicly available from the National Satellite Meteorological Center (NSMC) of China data service portal (https://data.nsmc.org.cn/DataPortal/en/home/index.html, accessed on 20 January 2025). The processed data and analysis codes supporting the findings of this study are publicly available at Zenodo: https://doi.org/10.5281/zenodo.18440339 (accessed on 1 February 2026).

Acknowledgments: We thank the anonymous reviewers for their constructive comments and suggestions.

Conflicts of Interest: The authors declare no conflicts of interest.

References

1. Lu, J. *An Introduction to Southwest Vortex*; China Meteorological Press: Beijing, China, 1986; pp. 63–64. (In Chinese)
2. Li, G. Advances in Tibetan Plateau Vortex and Southwest Vortex Research and Related Scientific Problems. *Desert Oasis Meteorol.* **2013**, *7*, 1–6. (In Chinese)
3. Li, Y.; Xu, X. A Review of the Research and Observing Experiment on Southwest China Vortex. *Adv. Meteorol. Sci. Technol.* **2016**, *6*, 134–140. (In Chinese)
4. Xiang, S.; Li, Y.; Zhai, S.; Peng, J. Comparative analysis of precipitation structures in two Southwest China Vortex events over eastern Sichuan Basin by TRMM. *J. Atmos. Sol.-Terr. Phys.* **2021**, *221*, 105691. [CrossRef]
5. Feng, X.; Liu, C.; Fan, G.; Liu, X.; Feng, C. Climatology and Structures of Southwest Vortices in the NCEP Climate Forecast System Reanalysis. *J. Clim.* **2016**, *29*, 7675–7701. [CrossRef]
6. Li, Y. Researches of the Vortex Source of Southwest China Vortex. *Plateau Meteorol.* **2021**, *40*, 1394–1406. (In Chinese)
7. Lai, X.; Wang, Q.; Huang, J. Progress in Climatological Research on the Southwest China Vortex. *Chin. J. Atmos. Sci.* **2023**, *47*, 1983–2000. (In Chinese)
8. Zheng, Q.; Xing, J. A Numerical Experiment on the Lee Cyclogenesis of Qinghai-Xizang Plateau in a Six-Level Limited Area Model. *Q. J. Appl. Meteorol.* **1990**, *1*, 12–23. (In Chinese)
9. Zhao, P.; Sun, S. Numerical Simulation and Diagnosis of the Formation of SW Vortex: An Analysis of Numerical Simulation of the Effects of Topography and Latent Heat on SW Vortex. *Sci. Atmos. Sin.* **1991**, *15*, 46–52. (In Chinese)
10. Wang, Q.; Tan, Z. Multi-scale topographic control of southwest vortex formation in Tibetan Plateau region in an idealized simulation. *J. Geophys. Res. Atmos.* **2014**, *119*, 11543–11561. [CrossRef]
11. Liu, C.; Li, Y.; Liu, Z.; Ye, M. Physical Formation Mechanisms of the Southwest China Vortex. *Atmosphere* **2022**, *13*, 1546. [CrossRef]
12. Wang, X.; Zhang, X.; Sun, J.; Lv, L.; Xu, W. The analysis on the structure characteristics of the Southwest Vortex in a rainstorm event in July 2008 over Huanghuai valley. *Torr. Rain Dis.* **2015**, *34*, 54–63. (In Chinese)
13. Zhang, Z.; Lin, M.; Qi, P.; Chen, S.; Wang, C. Numerical Simulation About Thermal Forcing Effect on Southwest Vortex's Developing Mechanism. *J. Arid Meteorol.* **2016**, *34*, 533–539. (In Chinese)
14. Li, L.; Zhang, R.; Wen, M. Genesis of southwest vortices and its relation to Tibetan Plateau vortices. *Q. J. Meteorol. Soc.* **2017**, *143*, 2556–2566. [CrossRef]
15. Xiao, Y.; Yu, S.; Gao, W.; Xiao, D.; Xiao, H.; Shi, R. Cause analysis of one sustained into-the-sea Plateau Vortex accompanied by Southwest Vortex. *Plateau Meteorol.* **2018**, *37*, 1616–1627. (In Chinese)
16. Yu, S.; Gao, W.; Peng, J. Analysis of influencing factors on frequent occurrence causes of Southwest China vortexes with different vortex sources from 2012 to 2017. *Torr. Rain Dis.* **2021**, *40*, 577–588. (In Chinese)
17. Chen, Y.; Li, Y. A thermodynamic condition affecting the movement of a southwest China vortex case. *Meteorol. Atmos. Phys.* **2022**, *134*, 36. [CrossRef]
18. Dong, Y.; Li, G.; Jiang, X.; Wang, Y. The characteristics and formation mechanism of double-band radar echoes formed by a severe rainfall occurred in the Sichuan Basin under the background of two vortices coupling. *Front. Earth Sci.* **2022**, *10*, 915954. [CrossRef]
19. Wang, X.; Liu, Y. Causes of extreme rainfall in May 2013 over Henan Province: The role of the southwest vortex and low-level jet. *Theor. Appl. Climatol.* **2017**, *129*, 701–709. [CrossRef]
20. Yang, K.; Xiao, D.; Jiang, X.; Li, Z.; Fu, S. Mechanisms Governing the Formation and Long-Term Sustainment of a Northeastward Moving Southwest Vortex. *Sustainability* **2023**, *15*, 9255. [CrossRef]
21. Li, J.; Chen, B.; Gao, G.; Li, Y. Development of Southwest Vortex and Rainstorm Triggering Mechanism under Two Kinds of Unstable Conditions. *Plateau Mountain Meteorol. Res.* **2023**, *43*, 1–10.
22. Zhou, C.; Li, Y. Dynamic and thermodynamic characteristics of warm-sector rainstorms caused by the southwest China vortex in Sichuan basin. *Theor. Appl. Climatol.* **2024**, *155*, 7095–7108. [CrossRef]
23. Ni, C.; Li, G.; Xiong, X. Analysis of a Vortex Precipitation Event over Southwest China Using AIRS and In Situ Measurements. *Adv. Atmos. Sci.* **2017**, *34*, 559–570. [CrossRef]
24. Mao, Z.; Liu, J. Classification of rainstorms in Hunan Province affected by the Southwest China vortex. *Torr. Rain Dis.* **2021**, *40*, 52–60. (In Chinese)
25. Wang, L.; Li, Y.; Xu, X.; Li, F. Characteristic Analysis of Dual-Polarization Weather Radar Echoes of Convective Precipitation and Snowfall in the Mount Everest Region. *Atmosphere* **2021**, *12*, 1671. [CrossRef]
26. Min, C.; Chen, S.; Gourley, J.; Chen, H.; Zhang, A.; Huang, Y.; Huang, C. Coverage of China New Generation Weather Radar Network. *Adv. Meteorol.* **2019**, *2019*, 5789358. [CrossRef]
27. Jiang, L.; Li, G.; Mu, L.; Kong, L. Structural Analysis of Heavy Precipitation Caused by Southwest Vortex Based on TRMM Data. *Plateau Meteorol.* **2014**, *33*, 607–614. (In Chinese)
28. Jiang, L.; Li, G.; Wang, X. Comparative study based on TRMM data of the heavy rainfall caused by the Tibetan Plateau vortex and the southwest vortex. *Sci. Atmos. Sin.* **2015**, *39*, 249–259. (In Chinese)

29. Li, G.; Chen, J. New progresses in the research of heavy rain vortices formed over the southwest China. *Torr. Rain Dis.* **2018**, *37*, 293–302. (In Chinese)
30. Xiang, J.; Wang, H.; Li, Z.; Bu, Z.; Yang, R.; Liu, Z. Case Study on the Evolution and Precipitation Characteristics of Southwest Vortex in China: Insights from FY-4A and GPM Observations. *Remote Sens.* **2023**, *15*, 4114. [CrossRef]
31. Byers, H.; Braham, R. Thunderstorm Structure and Circulation. *J. Atmos. Sci.* **1948**, *5*, 71–86. [CrossRef]
32. Houze, R. Mesoscale convective systems. *Rev. Geophys.* **2004**, *42*, RG4003. [CrossRef]
33. Houze, R. 100 Years of Research on Mesoscale Convective Systems. *Meteorol. Monogr.* **2018**, *59*, 17.1–17.54. [CrossRef]
34. Zhang, A.; Fu, Y. Life cycle effects on the vertical structure of precipitation in East China measured by Himawari-8 and GPM DPR. *Mon. Weather Rev.* **2018**, *146*, 2183–2199. [CrossRef]
35. Sun, Y.; Dong, X.; Cui, W.; Zhou, Z.; Fu, Z.; Zhou, L.; Deng, Y.; Cui, C. Vertical structures of typical Meiyu precipitation events retrieved from GPM-DPR. *J. Geophys. Res. Atmos.* **2020**, *125*, e2019JD031466. [CrossRef]
36. Zhou, M.; Liu, L.; Wang, H. Analysis of the Echo Structure and Its Evolution as Shown in a Severe Precipitation Event Caused by the Plateau Vortex and the Southwest Vortex. *Acta Meteorol. Sin.* **2014**, *72*, 554–569.
37. Pu, X.; Bai, A.; Mao, X. Analysis of the Process of Heavy Rain and Cloud System Characteristics Caused by the Interaction of the Plateau Vortex and the Southwest Vortex. *Adv. Meteorol. Sci. Technol.* **2021**, *94*, 1653–1660. (In Chinese)
38. He, Y.; Zhao, P.; Xiao, H.; Zhao, C. Structural difference on the response of microphysical and precipitation processes to aerosol perturbation in a quasi-stationary Southwest Vortex system. *J. Geophys. Res. Atmos.* **2025**, *130*, e2024JD041767. [CrossRef]
39. Matsui, T.; Iguchi, T.; Li, X.; Han, M.; Tao, W.; Petersen, W.; L'Ecuyer, T.; Meneghini, R.; Olson, W.; Kummerow, C.D.; et al. GPM satellite simulator over ground validation sites. *Bull. Am. Meteorol. Soc.* **2013**, *94*, 1653–1660. [CrossRef]
40. Hamada, A.; Takayabu, Y. Improvements in detection of light precipitation with the global precipitation measurement dual-frequency precipitation radar (GPM DPR). *J. Atmos. Ocean Technol.* **2016**, *33*, 653–667. [CrossRef]
41. Chandrasekar, V.; Le, M. Evaluation of profile classification module of GPM-DPR algorithm after launch. In Proceedings of the 2015 IEEE International Geoscience and Remote Sensing Symposium (IGARSS), Milan, Italy, 26–31 July 2015; pp. 5174–5177.
42. Petracca, M.; D'Adderio, L.; Porcù, F.; Vulpiani, G.; Sebastianelli, S.; Puca, S. Validation of GPM dual-frequency precipitation radar (DPR) rainfall products over Italy. *J. Hydrometeorol.* **2018**, *19*, 907. [CrossRef]
43. Zhang, A.; Fu, Y. The structural characteristics of precipitation cases detected by dual-frequency radar of GPM satellite. *Chin. J. Atmos. Sci.* **2018**, *42*, 33–51. (In Chinese)
44. Radhakrishna, B.; Satheesh, S.K.; Rao, T.N.; Saikranthi, K.; Sunilkumar, K. Assessment of DSDs of GPM-DPR with Ground-Based Disdrometer at Seasonal Scale over Gadanki, India. *J. Geophys. Res. Atmos.* **2016**, *121*, 11792–11802. [CrossRef]
45. Chandrasekar, V.; Biswas, S.K.; Le, M.; Chen, H. Cross Validation of Raindrop Size Distribution Retrievals from GPM Dual-frequency Precipitation Radar Using Ground-based Polarimetric Radar. In Proceedings of the 2018 IEEE International Geoscience and Remote Sensing Symposium (IGARSS), Valencia, Spain, 22–27 July 2018; pp. 8335–8338.
46. Peinó, E.; Bech, J.; Polls, F.; Udina, M.; Petracca, M.; Adirosi, E.; Gonzalez, S.; Boudevillain, B. Validation of GPM DPR Rainfall and Drop Size Distributions Using Disdrometer Observations in the Western Mediterranean. *Remote Sens.* **2024**, *16*, 2594. [CrossRef]
47. Chen, P.; Chen, L.; Wang, G.; Wu, Q.; Wang, H.; Zhang, P. Comparison of reflectivity consistency between spaceborne precipitation radar and ground-based weather radar in China and the United States. *Adv. Atmos. Sci.* **2025**, *42*, 1376−1394. [CrossRef]
48. Li, X.; Wu, C.; Jiang, X. Complex Terrain Calibration Method for Ground-based Radar in Sichuan Based on Spaceborne Radar. *J. Appl. Meteorol. Sci.* **2026**, *37*, 41–55. (In Chinese)
49. Li, J.; Zheng, J.; Liu, Y.; Cheng, Z.; He, J.; Ren, T.; Chen, S. A study on vertical structure and macro- to micro-characteristics and differences of precipitation in Sichuan basin and the surrounding areas. *Acta Meteorol. Sin.* **2022**, *80*, 205–223. (In Chinese)
50. China Meteorological Administration Chengdu Plateau Meteorology Institute; Chinese Meteorological Society Plateau Meteorology Committee. *Southwest Vortex Yearbook 2013*, 1st ed.; Science Press: Beijing, China, 2015. (In Chinese)
51. Wang, J.; Chen, J.; Zhang, J.; Zhang, H.; Wang, J. A new method for gradually identifying the southwest vortex. *Trans. Atmos. Sci.* **2019**, *42*, 621–630. (In Chinese)
52. Wang, J.; Li, D.; Wang, Y. Characteristics reanalysis on southwest vortex. *J. Meteorol. Sci.* **2015**, *35*, 133–139. (In Chinese)
53. Dong, Y.; Jiang, X.; Lu, P.; Xiao, D.; Feng, Y.; Zhang, K. A New Objective Identification Method of the Southwest Vortex Based on Reanalysis Grid Data and Its Effect Evaluation. *Chin. J. Atmos. Sci.* **2024**, *48*, 2125–2140. (In Chinese)
54. Williams, M.; Houze, R. Satellite-Observed Characteristics of Winter Monsoon Cloud Clusters. *Mon. Weather Rev.* **1987**, *115*, 505–519. [CrossRef]
55. Machado, L.; Rossow, W.; Guedes, R.; Walker, A. Life cycle variations of mesoscale convective systems over the Americas. *Mon. Weather Rev.* **1998**, *126*, 1630–1654. [CrossRef]
56. Wang, H.; Tan, L.; Zhang, F.; Zheng, J.; Liu, Y.; Zeng, Q.; Yan, Y.; Ren, X.; Xiang, J. Three-Dimensional Structure Analysis and Droplet Spectrum Characteristics of Southwest Vortex Precipitation System Based on GPM-DPR. *Remote Sens.* **2022**, *14*, 4063. [CrossRef]

57. Yang, Y.; Zhao, C.; Wang, Y.; Sun, Y.; Fan, H.; Zhao, X.; Zhou, Y. Evolution characteristics of convective clouds with relatively small scales over South China. *J. Geophys. Res. Atmos.* **2024**, *129*, e2024JD040780. [CrossRef]
58. Huo, Z.; Ruan, Z.; Wei, M.; Ge, R.; Li, F.; Ruan, Y. Statistical characteristics of raindrop size distribution in south China summer based on the vertical structure derived from VPR-CFMCW. *Atmos. Res.* **2019**, *22*, 47–61. [CrossRef]
59. Huang, Y.; Ruan, Z.; Guo, X. The classification statistics on summer precipitation in Beijing using vertical sounding radar. *Plateau Meteorol.* **2016**, *35*, 745–754. (In Chinese)
60. Fu, Y.; Liu, Q.; Zi, Y.; Feng, S.; Li, Y.; Liu, G. Summer Precipitation and Latent Heating over the Tibetan Plateau Based on TRMM Measurements. *Plateau Mt. Meteorol. Res.* **2008**, *28*, 1674–2184. (In Chinese)
61. Houze, R. Stratiform precipitation in regions of convection: A meteorological paradox? *Bull. Am. Meteorol. Soc.* **1997**, *78*, 2179–2196. [CrossRef]
62. Yuter, S.; Houze, R. Three-dimensional kinematic and microphysical evolution of Florida cumulonimbus. Part I: Spatial distribution of updrafts, downdrafts, and precipitation. *Mon. Weather Rev.* **1995**, *123*, 1921–1940. [CrossRef]
63. Wu, D.; Zhao, K.; Kumjian, M.R.; Chen, X.; Huang, H.; Wang, M.; Didlake, A.; Duan, Y.; Zhang, F. Kinematics and microphysics of convection in the outer rainband of Typhoon Nida (2016) revealed by polarimetric radar. *Mon. Weather Rev.* **2018**, *146*, 2147–2159. [CrossRef]
64. Du, S.; Wang, D.; Li, G.; Cai, Q.; Xu, X. Analysis of the Vertical Structure of Precipitation in South China Based on Dual-Frequency Spaceborne Precipitation Radar GPM Product. *J. Trop. Meteorol.* **2020**, *36*, 115–130. (In Chinese)
65. Kumjian, M.; Prat, O. The impact of raindrop collisional processes on the 451 polarimetric radar variables. *J. Atmos. Sci.* **2014**, *71*, 3052–3067. [CrossRef]
66. Wen, L.; Chen, G.; Yang, C.; Zhang, H.; Fu, Z. Seasonal variations in precipitation microphysics over East China based on GPM DPR observations. *Atmos. Res.* **2023**, *293*, 106933. [CrossRef]
67. Yang, J.; Li, Y.; Hu, X.; Zhang, Z.; Kou, X. Microphysical Characteristics of Convective and Stratiform Precipitation Generated at Different Life Stages of Precipitating Cloud in the Pre-Summer Rainy Season in South China. *Remote Sens.* **2025**, *17*, 1250. [CrossRef]
68. Guilloteau, C.; Foufoula-Georgiou, E. Life Cycle of Precipitating Cloud Systems from Synergistic Satellite Observations: Evolution of Macrophysical Properties and Precipitation Statistics from Geostationary Cloud Tracking and GPM Active and Passive Microwave Measurements. *J. Hydrometeorol.* **2024**, *25*, 789–805. [CrossRef]
69. Li, D.; Qi, Y.; Li, H. Statistical characteristics of convective and stratiform precipitation during the rainy season over South China based on GPM-DPR observations. *Atmos. Res.* **2024**, *301*, 107267. [CrossRef]

Disclaimer/Publisher's Note: The statements, opinions and data contained in all publications are solely those of the individual author(s) and contributor(s) and not of MDPI and/or the editor(s). MDPI and/or the editor(s) disclaim responsibility for any injury to people or property resulting from any ideas, methods, instructions or products referred to in the content.